Control of Ca^{2+} signals by astrocyte nanoscale morphology at tripartite synapses

Running Title: Astrocyte morphology tunes Ca2+ signals

Audrey Denizot [1*], Misa Arizono[2,3], Valentin U. Nägerl[2,3], Hugues Berry[4,5], Erik De Schutter[1]

[1] Okinawa Institute of Science and Technology, Computational Neuroscience Unit, Onna-Son, Japan

[2] Interdisciplinary Institute for Neuroscience, Université de Bordeaux, Bordeaux, France

[3] Interdisciplinary Institute for Neuroscience, CNRS UMR 5297, Bordeaux, France

[4] Univ Lyon, LIRIS, UMR5205 CNRS, F-69621, Villeurbanne, France

[5] INRIA, F-69603, Villeurbanne, France

Corresponding author: audrey.denizot3@oist.jp

Acknowledgements: This work was funded by the Okinawa Institute of Science and Technology Graduate University and by JSPS (Japan Society for the Promotion of Science) Postdoctoral Fellowship for Research in Japan (Standard, P21733). We thank Iain Hepburn and Weiliang Chen of the Computational Neuroscience Unit, OIST, Japan for discussion on 3D meshes and STEPS.

Data availability statement: The simulation code and meshes used in this study are available at http://modeldb.yale.edu/266928, access code: lto42@tpk3D?.

Conflict of Interest Statement: The authors declare no competing financial interests.

Word Count: 5752

Abstract: 206, **Introduction:** 640, **Methods:** 2377, **Results:** 1875, **Discussion:** 727

Abstract

Much of the Ca^{2+} activity in astrocytes is spatially restricted to microdomains and occurs in fine processes that form a complex anatomical meshwork, the so-called spongiform domain. A growing body of literature indicates that those astrocytic Ca^{2+} signals can influence the activity of neuronal synapses and thus tune the flow of information through neuronal circuits. Because of technical difficulties in accessing the small spatial scale involved, the role of astrocyte morphology on Ca^{2+} microdomain activity remains poorly understood. Here, we use computational tools and idealized 3D geometries of fine processes based on recent super-resolution microscopy data to investigate the mechanistic link between astrocytic nanoscale morphology and local Ca^{2+} activity. Simulations demonstrate that the nano-morphology of astrocytic processes powerfully shapes the spatio-temporal properties of Ca^{2+} signals and promotes local Ca^{2+} activity. The model predicts that this effect is attenuated upon astrocytic swelling, hallmark of brain diseases, which we confirm experimentally in hypo-osmotic conditions. Upon repeated neurotransmitter release events, the model predicts that swelling hinders astrocytic signal propagation. Overall, this study highlights the influence of the complex morphology of astrocytes at the nanoscale and its remodeling in pathological conditions on neuron-astrocyte communication at so-called tripartite synapses, where astrocytic processes come into close contact with pre- and postsynaptic structures.

Keywords

Intracellular signaling, calcium microdomains, nano-morphology, computational neuroscience, reaction-diffusion simulations

Table of Contents

Main Points

- Astrocyte nano-morphology favors the compartmentalization of biochemical signals
- This compartmentalization promotes local Ca^{2+} activity and signal propagation robustness
- In contrast, its pathological remodeling upon swelling attenuates Ca^{2+} activity

Table of Contents Image

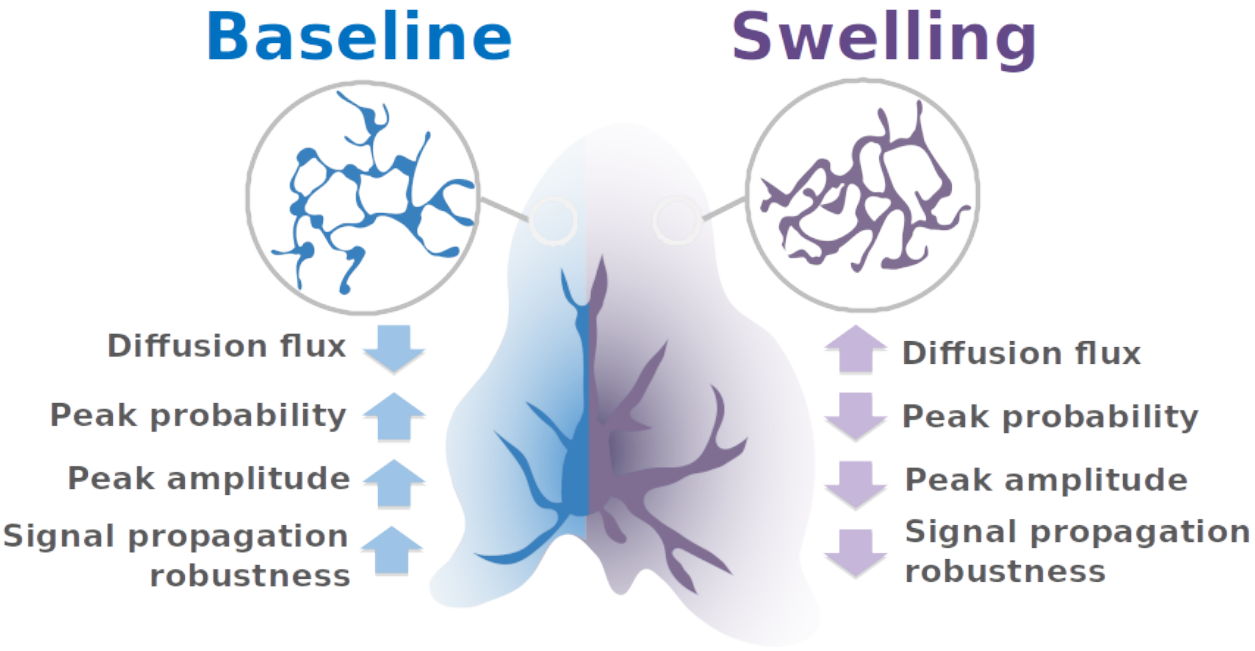

Figure 1: **Proposed mechanisms that regulate astrocytic Ca^{2+} activity in perisynaptic astrocytic processes.** Our simulation results demonstrate that the nano-morphology of astrocytic processes, consisting in the alternation of nodes and shafts, favors the compartmentalization of biochemical signals. This compartmentalization promotes local Ca^{2+} activity and signal propagation robustness. Astrocyte swelling, observed in pathological conditions such as brain injury, stroke and epilepsy, results in an increased shaft width without altering node size. Our results suggest that such pathological alterations of the nanoscale morphology of astrocytes result in a decreased local Ca^{2+} activity, which we confirm experimentally in hypo-osmotic conditions. Upon repeated neuronal stimuli, we predict that swelling hinders astrocytic signal propagation. Overall, this study highlights the impact of astrocyte nano-morphology on astrocyte activity at tripartite synapses, in health and disease.

Main Text

Introduction

Astrocytes are glial cells of the central nervous system that are essential for brain development and function Verkhratsky & Nedergaard (2018). They notably modulate neuronal communication at synapses. Astrocytic Ca^{2+} signals are triggered by neurotransmitters released by active neurons, which can trigger the release of neuroactive molecules by the astrocyte, referred to as gliotransmitters. The first type of astrocytic Ca^{2+} signals that has been observed was Ca^{2+} waves that propagate through gap junctions

in astrocyte networks Giaume & Venance (1998). Ca^{2+} waves have also been observed in the branches of single astrocytes, sporadically propagating to the soma Haustein et al. (2014); Bindocci et al. (2017). The recent development of Ca^{2+} imaging techniques with improved spatial and temporal resolution has revealed the existence of spatially-restricted Ca^{2+} signals in astrocytes, referred to as microdomains or hotspots Di Castro et al. (2011); Panatier et al. (2011); Stobart, Ferrari, Barrett, Glück, et al. (2018); Srinivasan et al. (2015); Shigetomi et al. (2013); Sherwood et al. (2017); Otsu et al. (2015); Lind et al. (2013); Bindocci et al. (2017); Agarwal et al. (2017); Arizono et al. (2020); Otsu et al. (2015). These local Ca^{2+} signals account for the vast majority ($\approx$ 80 %) of astrocytic Ca^{2+} activity and occur in fine processes, which occupy 75 % of the astrocytic volume Bindocci et al. (2017), forming the spongiform domain, also referred to as the gliapil. Given that one astrocyte may contact tens of thousands of synapses simultaneously Bushong et al. (2002) via these fine processes, local and fast Ca^{2+} signals might enable the astrocyte to powerfully yet precisely control the flow of information through synaptic circuits. Importantly, reactive astrocytes, hallmark of brain diseases, display aberrant amplitude, duration, frequency and spatial spread of Ca^{2+} signals Shigetomi et al. (2019); Nedergaard et al. (2010); Lee et al. (2022).

Cellular micro-morphology lends itself to the compartmentalization of biochemical signals. For example, the anatomical design of dendritic spines restricts the diffusion of Ca^{2+} to the activated synapse, which reduces cross-talk between nearby synapses Santamaria et al. (2011); Tonnesen et al. (2014); Yuste et al. (2000); Noguchi et al. (2005); Yasuda (2017); Holcman & Schuss (2011). The complex shapes of Bergmann glia Grosche et al. (1999) and perisynaptic "astrocytic compartments" along major branches Panatier et al. (2011) have been proposed to restrict Ca^{2+} signals to the vicinity of synapses. Fine processes of the spongiform domain, however, cannot be resolved by diffraction-limited light microscopy Rusakov (2015), so that the contribution of their morphology to shaping local Ca^{2+} signals is poorly understood. Our recent 3D STED study Arizono et al. (2020) revealed the structural basis of compartmentalized spontaneous Ca^{2+} signals in fine astrocytic processes. Importantly, pathological changes in astrocytic morphology Lafrenaye & Simard (2019), such as "astrocytic swelling", are paired with aberrant Ca^{2+} signals Shigetomi et al. (2019). We have recently reported that swelling can also occur at the level of fine astrocytic processes Arizono, Bancelin, et al. (2021). The effect of such a remodeling of astrocytic nano-morphology on the local Ca^{2+} signals involved in regulating synapses remains yet unclear. Together, there is a great interest in understanding the mechanistic link between the nano-morphology of astrocytic processes and Ca^{2+} profiles in health and disease. Computational approaches make it possible to simulate different geometrical scenarios, in a much more systematic and controlled way than what could be done experimentally. Computational

models can thus help us gain insights into the impact of morphological parameters on Ca^{2+} activity.

Here, we use computational tools to explore the role of the anatomical design of the gliapil. To do so, we perform simulations in branchlet geometries that we designed based on super-resolution microscopy data reported in live tissue Arizono et al. (2020), consisting of nodes, which host Ca^{2+} microdomains, and their intervening shafts of variable widths. Our simulation results suggest that the nanoscale design of the spongiform domain effectively decreases diffusion flux, which increases Ca^{2+} peak probability, duration and amplitude in the stimulated and neighboring nodes. To test those predictions, we performed Ca^{2+} recordings in organotypic hipppocampal cultures in hypo-osmotic conditions,where the normal node-shaft arrangement is altered. In line with our model predictions, Ca^{2+} activity in hypo-osmotic conditions was decreased compared to Ca^{2+} activity in normal tissue. We further found that, upon repeated neuronal stimulation, thin shafts allow signal propagation even if some stimuli are omitted, thus allowing for a more robust signal propagation.

Overall, our study sheds light on the influence of the nanoscale morphology of the complex spongiform domain of astrocytes on Ca^{2+} microdomain activity and indicates that pathological morphological changes may substantially affect their Ca^{2+} activity.

Methods

Stochastic spatially-explicit voxel-based simulations

In order to model astrocyte Ca^{2+} signals in astrocyte branchlets, we have used the voxel-based "GCaMP" implementation of the Inositol 3-Phosphate (IP_3) receptor-dependent Ca^{2+} signaling model from Denizot et al Denizot et al. (2019), using the same reaction scheme and parameter values (Fig 2B). Briefly, we model Ca^{2+} fluxes in and out of the cytosol, mediated by Ca^{2+} channels and pumps on the endoplasmic reticulum (ER) and on the plasma membrane. Ca^{2+} signals occur when some IP_3R channels are in the open state. IP_3 can be synthesized by the Ca^{2+}-dependent activity of phospholipase C δ (PLCδ) and the removal of IP_3 molecules from the cytosol is expressed as a single decay rate. IP_3R kinetics is described by a Markov model, derived from De Young & Keizer's model De Young & Keizer (1992). Each IP_3R molecule contains one IP_3 binding site and two Ca^{2+} binding sites. An IP_3R is in the open state when in state {110} (first Ca site and IP_3 bound, second Ca site free). Depending on the simulation, other diffusing molecules were added to the model, such as the fluorescent molecule ZsGreen and fluorescent Ca^{2+} indicators, here 10 μM of GCaMP6s.

GCaMPs are genetically-encoded Ca^{2+} indicators (GECIs) that are derived from the fluorescent protein GFP and the Ca^{2+} buffer calmodulin (see Shigetomi et al. (2016) for a review on GECIs). For further details on the kinetic scheme and model assumptions, please refer to Denizot et al. 2019 Denizot et al. (2019).

The model was implemented using STEPS (http://steps.sourceforge.net/), a python package performing exact stochastic simulation of reaction-diffusion systems Hepburn et al. (2012). More presicely, STEPS uses a spatialized implementation of Gillespie's SSA algorithm Gillespie (1977); Isaacson & Isaacson (2009); Smith & Grima (2018). Simulations in STEPS can be performed in complex geometries in 3 spatial dimensions. Space is divided into well-mixed tetrahedral compartments, referred to as voxels. Reactions between 2 molecules can only occur if they are located within the same voxel. Diffusion events are modeled as a decrease of the number of molecules in the original voxel and an increase in the number of molecules in its neighboring voxel. Boundary conditions, except when specified otherwise, were reflective. In other words, mobile molecules could not diffuse away from the geometry, as if they were "bouncing" onto the plasma membrane. STEPS enables to compute, in complex 3D geometries, reactions and diffusion in the cytosol as well as reactions between cytosolic molecules and molecules located at the plasma or ER membrane.

Geometries

Typical astrocyte branchlet geometries were designed from their recent experimental characterization in live tissue at high spatial resolution (50 nm in x-y) Arizono et al. (2020). Those geometries consist in alternations of bulbous structures, nodes, connected to each other with cylindrical structures, shafts. Geometries with different shaft widths d_{shaft} were designed using Trelis software (https://www.csimsoft.com/trelis, Fig 2A). The geometry of a node was approximated as being a sphere of diameter 380 nm. Shaft geometry consisted in a 1μm long cylinder. Shaft diameter was defined relative to node diameter. For example, shaft diameter was the same as node diameter, i.e $d_{shaft} = d_0$=380 nm. Similarly, shaft diameter was 190 nm and 127 nm for $d_{shaft} = \frac{d_0}{2}$ and $\frac{d_0}{3}$, respectively. Cones were positioned between spheres and cylinders in order to create a smoother transition between nodes and shafts, better approximating the geometry observed experimentally. Cytosolic volume was thus V_1=0.620 μm^3, V_2=0.263 μm^3 and V_3=0.195 μm^3, for $d_{shaft} = d_0$, $\frac{d_0}{2}$ and $\frac{d_0}{3}$, respectively. A subset of simulations was performed in a geometry with V_1=0.258 μm^3. This geometry is characterized, similarly to geometries with $d_{shaft} = d_0$, by a node/shaft width ratio of 1. It contains cylinders of length 750 nm, diameter 285 nm and spheres of diameter 285 nm. As a first approximation, ER geometry was considered to be similar to the geometry of the astrocyte branchlet: node/shaft successions.

ER nodes were aligned with cytosolic nodes. As no quantification of the ratio between astrocytic ER volume and cellular volume was found in the literature, ER volume was 10% of the total branchlet volume, based on available data in neurons Spacek & Harris (1997). As the shape and distribution of the ER in fine processes have not been characterized in live tissue but are likely highly variable, additional simulations were performed in meshes with various ER shapes: "No ER", "Node ER" and "Cyl ER", in which there was no ER, discontinuous ER in nodes or cylindrical ER, respectively (Fig S7-S9). The cytosolic volume, plasma and ER membrane surface areas of those 3D geometries are presented in Table 1.

A sensitivity study was performed to investigate the effect of voxel size on the kinetics of the molecular interactions modeled. Information on the voxel sizes of the different meshes used is presented in Table S1. Results are presented in Figure S1. Meshes that contained voxels that were < 50 nm^3 were characterized by aberrant kinetics, resulting in aberrant average numbers of molecules in a given state. Those results thus suggest that to prevent errors due to voxel size, meshes should not display voxel sizes that are< 50 nm^3. We have thus made sure, while meshing the geometries in which simulations were ran, that no voxels were < 50 nm^3. Minimum voxel size was 443 nm^3, 1100 nm^3 and 447 nm^3, for $\mathrm{d_{shaft}} = d_0$, $\frac{d_0}{2}$ and $\frac{d_0}{3}$ geometries, respectively.

In a subset of simulations, ER geometry varied. The shape of the cell was the same as in "5nodes" geometries (Fig 2). ER geometry consisting of node/shaft alternations, described above, is referred to as "Node/shaft ER". "No ER" geometry contains no ER. "Node ER" is characterized by a discontinuous ER geometry, consisting in spheres of diameter 54 nm, located in cellular nodes. "Cyl ER" corresponds to a cylindrical ER, of length $l_{\mathrm{ER}} = 6274$ nm and a diameter of 108, 54 and 36 nm, for $\mathrm{d_{shaft}} = d_0$, $\frac{d_0}{2}$ and $\frac{d_0}{3}$, respectively. The associated cytosolic volume, ER and plasma membrane area are presented in Table 1.

Protocol for simulating bleaching experiments

In order to test whether the idealized geometries presented in Fig 2 are a good approximation of the spongiform ultrastructure of astrocyte branchlets, we have simulated their fluorescence recovery after photobleaching (FRAP) experiments. Briefly, laser pulses are simulated on a node (region of interest) while the fluorescence level is being recorded. At bleaching time, the fluorescence level in the region of interest decreases to I_0. Then, because of the diffusion of fluorescent molecules into the region of interest, fluorescence increases until it reaches a new steady state, I_{inf}. We characterize node compartmentalization by measuring the time τ taken by fluorescing molecules to diffuse into the node to reach I_{inf}. In other words,

a high node compartmentalization will be associated with a high value of τ. Thus, 3 main parameters characterize bleaching traces: I_0, τ and I_{inf}.

To mimic bleaching experiments in fine branchlets performed by Arizono et al Arizono et al. (2020), ZsGreen molecules were added to simulation space. After 2 seconds of simulation, providing the basal level of fluorescence, 60% of ZsGreen molecules were bleached. In order to fit I_0 and I_{inf} that were measured experimentally, and as bleaching time lasted 10 ms in experiments and 1 ms in simulations, the bleached volume in simulations was adjusted depending on the geometry (see Fig 3A). Bleaching was simulated as a transition from ZsGreen molecules to ZsGreen-bleached molecules, the latter being considered as non-fluorescing molecules. Screenshots of simulations, illustrating the diffusion of ZsGreen and ZsGreen-bleached molecules, are presented in Fig S2B. The number of ZsGreen molecules in the central node was recorded over simulation time and a fit was performed following equation 1 to determine the values of I_0, I_{inf} and τ.

$$I(t) = I_0 - (I_0 - I_{\text{inf}})e^{-\mathrm{t}/\tau} \tag{1}$$

, where I(t) is the level of fluorescence measured at time t. The coefficient of diffusion, D_{ZsGreen}, and the concentration, [ZsGreen], of ZsGreen were adjusted to fit experimental data. Indeed, the amplitude of [ZsGreen] fluctuations at steady state is inversely proportional to the number of ZsGreen molecules in the geometry. In other words, fluorescence signals are more noisy when [ZsGreen] is low. Moreover, the autocorrelation of those fluctuations depends on the coefficient of diffusion of ZsGreen, D_{ZsGreen}. If D_{ZsGreen} increases, the autocorrelation of Lag, where Lag is the autocorrelation delay, will decrease faster as Lag increases. Comparing the fluctuations of [ZsGreen] and its autocorrelation in experiments and in simulations thus enabled to find the values of D_{ZsGreen} and of [ZsGreen] that allowed for the best fit to experimental data. In the simulations presented here, D_{ZsGreen}=90 $\mu m^2.s^{-1}$ and [ZsGreen]=25 μM.

Protocols for simulating neuronal stimulation

In order to investigate the propagation of Ca^{2+} signals from nodes that contact neuronal spines, we have developed 2 different protocols for our simulations, performed in the geometries presented in Fig 2. As nodes were the site of Ca^{2+} signal initiation Arizono et al. (2020) and as most spines contacted nodes rather than shafts, we have simulated neuronal stimulation in nodes. To simulate neuronal stimulation, IP_3 and Ca^{2+} were infused in the cytosol at stimulation time. IP_3 infusion reflects the production of IP_3 by phospholipase C that results from the activation of G_q-G-protein-coupled receptors (GPCRs). Ca^{2+} infusion mimics the

influx of Ca^{2+} in the cytosol through Ca^{2+} channels at the plasma membrane. The rate of this neuronal activity-induced Ca^{2+} influx, k_{Ca}, varied within a physiological range of values, from 0 to 1000 s^{-1} Wu et al. (2018); Brazhe et al. (2018). Signals were recorded both in the stimulated node, Node 1, and in the neighboring node, Node 2.

- In the first protocol, 100 IP_3 molecules were infused in Node 1, at t=t_0=1s, while Ca^{2+} activity was monitored in Node 1 and in the neighboring node, Node 2 (see e.g Fig 4A). Neuronal activity-induced Ca^{2+} influx was mediated by generic Ca^{2+} channels at the plasma membrane. 25 of those Ca^{2+} channels were placed on the plasma membrane of Node 1, corresponding to a similar density to the IP_3R density on the ER membrane, and were set to an inactive state. At stimulation time t=t_0, Ca^{2+} channels were set to an active state, resulting in an influx of Ca^{2+} within the cytosol at rate k_{Ca}. At t=$t_0 + 1$, Ca^{2+} channels were set back to their initial inactive state. Simulations were performed in geometries with varying shaft width d_{shaft} .
- In the second protocol, we have investigated signal propagation in the node/shaft geometry depending on shaft width d_{shaft} when several nodes were successively stimulated. In "5nodes" geometries, 50 IP_3 molecules were infused at t_0=5s, $t_0 + \tau_{\text{IP3}}$, $t_0 + 2\tau_{\text{IP3}}$, $t_0 + 3\tau_{\text{IP3}}$ in Nodes 1, 2, 3 and 4, respectively. During the whole simulation time, Ca^{2+} activity was recorded in Node 5 (see Fig 6). In a subset of simulations, stimulation of Nodes 2, 3 and 4 occurred with a probability $1 - p_{\text{fail}}$, with $p_{\text{fail}} \in [0, 1]$.

Code accessibility

The simulation code, implemented with STEPS 3.5.0, and the meshes are available on ModelDB McDougal et al. (2017) at http://modeldb.yale.edu/266928, access code: lto42@tpk3D?. The original model from Denizot et al. Denizot et al. (2019) is available at http://modeldb.yale.edu/247694.

Peak detection and analysis

The same strategy as developed by Denizot et al. Denizot et al. (2019) was used for detecting and analysing Ca^{2+} signals. Briefly, basal concentration of Ca^{2+}, $[Ca]_{\text{b}}$, was defined based on a histogram of the number of Ca^{2+} ions in the absence of neuronal stimulation. Peak initiation corresponded to the time when [Ca^{2+}] was higher than the following threshold: $[Ca]_{\text{b}} + n\sigma_{\text{Ca}}$, where σ_{Ca} is the standard deviation of [Ca^{2+}] histogram in the absence of neuronal stimulation. The value of n was set by hand depending on signal/noise ratio of the simulation of interest. Peak termination corresponded to the time when [Ca^{2+}] decreased below the peak threshold.

Several parameters were analyzed to characterize Ca^{2+} signals. Peak amplitude, A, corresponds to the maximum [Ca^{2+}] measured during the peak duration. It is expressed as signal to noise ratio $SNR = \frac{A-[Ca]_b}{[Ca]_b}$. Peak duration corresponds to the time between peak initiation and peak termination. Time to 1^{st} peak corresponds to the delay between the beginning of the simulation and the first peak detection, measured in the cellular compartment of interest. Peak probability corresponds to the fraction of simulations in which at least one peak was detected during simulation time in the region of interest. Ca^{2+} residency time was measured by performing n=300 simulations for each value of d_{shaft} , in which only 1 Ca^{2+} ion was added to node 1, without other molecular species. Ca^{2+} residency time corresponds to the time taken for the ion to diffuse away from node 1.

Organotypic hippocampal slice cultures

All experiments were performed as described in Arizono et al. (2020) and were in accordance with the European Union and CNRS UMR5297 institutional guidelines for the care and use of laboratory animals (Council directive 2010/63/EU). Organotypic hippocampal slices (Gähwiler type) were dissected from 5–7-d-old wild-type mice and cultured 5–8 week in a roller drum at 35°C, as previously described Gähwiler (1981).

Viral infection

AAV9-GFAP-GCaMP6s Stobart, Ferrari, Barrett, Stobart, et al. (2018) was injected by brief pressure pulses (40ms; 15 psi) into the stratum radiatum of 2-3-week old slices from Thy1-YFP-H (JAX:003782) mice 4-6 weeks prior to the experiment.

Image acquisition

For Ca^{2+} imaging, we used a custom-built setup based on an inverted microscope body (Leica DMI6000), as previously described in Tonnesen et al. (2011). We used a 1.3 NA glycerol immersion objective equipped with a correction collar to reduce spherical aberrations and thereby allow imaging deeper inside brain tissue Urban et al. (2011). The excitation light was provided by a pulsed diode laser (l = 485 nm, PicoQuant, Berlin, Germany). The fluorescence signal was confocally detected by an avalanche photodiode (APD; SPCM-AQRH-14-FC; PerkinElmer). The spatial resolution of the setup was around 200 nm (in x-y) and 600 nm (z). Confocal time-lapse imaging (12.5 x 25 μm, pixel size 100 nm) was performed at 2Hz for 2.5 min in artificial cerebrospinal fluid containing 125 mM NaCl, 2.5 mM KCl, 1.3 mM $MgCl_2$, 2 mM $CaCl_2$, 26 mM $NaHCO_3$, 1.25 mM NaH_2PO_4, 20 mM D-glucose, 1 mM Trolox; 300 mOsm; pH 7.4. Perfusion rate was 2 mL/min and the temperature 32 °C. Hypo-osmotic stress (300 mOsm to 200 mOsm) was applied by perfusing

ACSF with reduced NaCl concentration (119 to 69 mM NaCl).

Experimental Design and Statistical Analysis

For each parameter set, 20 simulations, with different seeds, were generated. Each parameter describing Ca^{2+} dynamics was expressed as mean ± standard deviation. The effect of d_{shaft} on each Ca^{2+} signal characteristic was tested using one-way ANOVA. Comparison between two different conditions was performed using unpaired Student T-test if values followed a Gaussian distribution, Mann-Whitney test otherwise. Significance is assigned by * for $p \leq 0.05$, ** for $p \leq 0.01$, *** for $p \leq 0.001$.

Results

Geometrical representation of typical astrocyte processes

In order to investigate the role of the nano-morphology of astrocytic processes on the spatio-temporal properties of Ca^{2+} microdomains, we have designed geometries of typical astrocyte processes, derived from our recent characterization of their ultrastructure at a high spatial resolution (50 nm in x-y) in organotypic hippocampal culture as well as in acute slices and *in vivo* Arizono et al. (2020) (Fig 2A). Geometries consist of alternations of bulbous structures, nodes, connected to each other via cylindrical structures, referred to as shafts. To reproduce the morphological changes of processes associated with cell swelling reported in hypo-osmotic conditions (Fig 3 in Arizono, Inavalli, et al. (2021)), geometries with different shaft width d_{shaft} and constant node width were designed (Fig 2B). In accordance with node-shaft structures observed experimentally Arizono et al. (2020), node width was set to 380 nm. To model astrocytic Ca^{2+} activity with a high spatial resolution while taking into account the randomness of reactions in small volumes, we used the stochastic voxel-based model from Denizot et al. Denizot et al. (2019). The reactions included in the model are presented in Fig 2C and in the Methods section. As the majority of Ca^{2+} signals in astrocytes result from the opening of Inositol 3-Phosphate receptors (IP_3Rs), located at the membrane of the endoplasmic reticulum (ER) Srinivasan et al. (2015), signals in the model result from the opening of IP_3Rs (see Denizot et al. Denizot et al. (2019) for discussion on the model's assumptions and limitations).

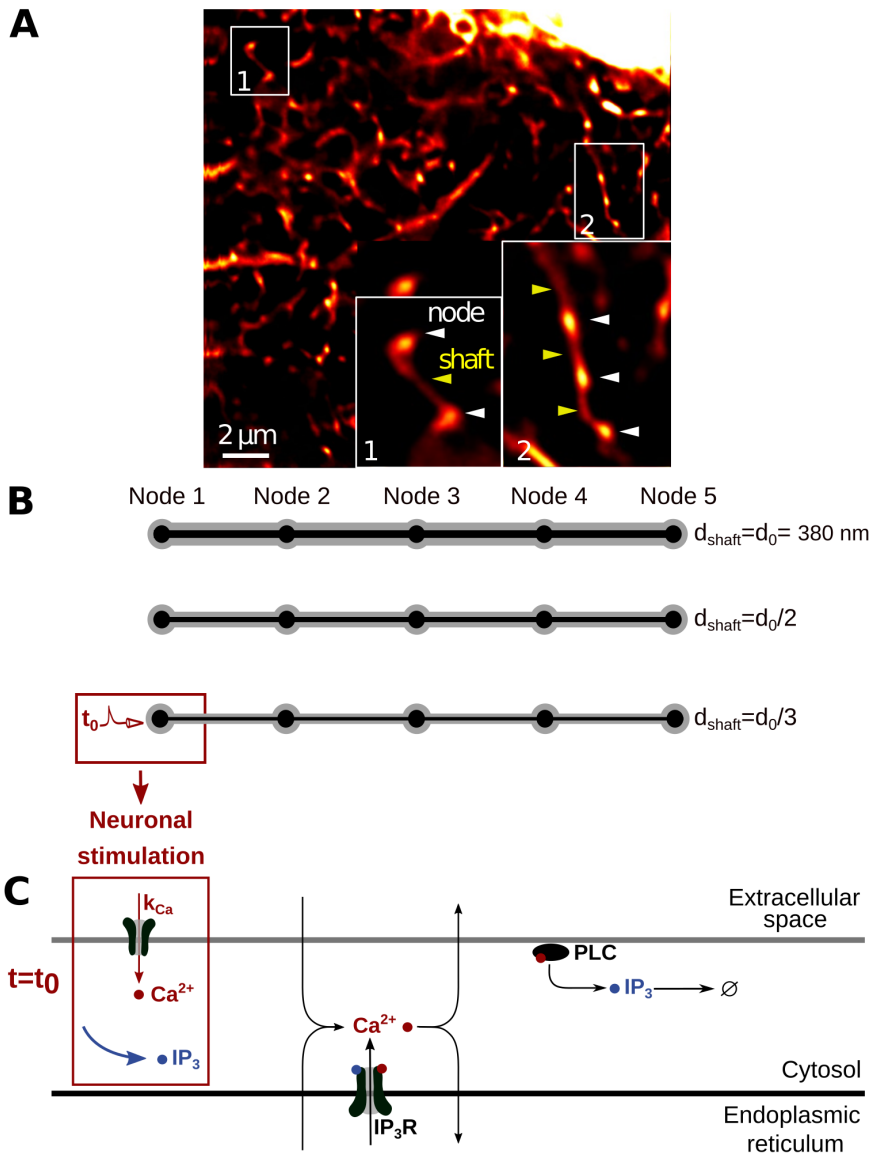

Figure 2: **Geometries and kinetic scheme used for simulating Ca^{2+} dynamics in node/shaft structures of the gliapil.**

Thin shafts favor node compartmentalization

In order to test whether the geometries designed in this study are a good approximation of the ultrastructure of the gliapil, we have compared molecular diffusion flux in those geometries with those reported experimentally. To do so, we simulated photobleaching experiments and compared our results to experimental results from Arizono et al. Arizono et al. (2020). The principle of bleaching simulations is presented in the Methods section and in Movie S1. Here, we refer to an increased node compartmentalization when the time

to recovery after bleaching, τ, increases (see Fig 3B).

Bleaching traces in simulations are both qualitatively (Fig 3B) and quantitatively (Fig 3C) similar to experimental bleaching traces, for shaft width $d_{\text{shaft}} = d_0$ and $d_{\text{shaft}} = \frac{d_0}{2}$. Indeed, no significant difference of I_0 (Fig 3C1), I_{inf} (Fig 3C2) and τ (Fig 3C3) was observed between simulations and experimental traces. Simulations were also performed with $d_{\text{shaft}} = \frac{d_0}{3}$. Our simulations successfully reproduce experimental bleaching experiments and suggest that τ, and thus node compartmentalization, increases when shaft width decreases (Fig 3C3). This result is not surprising as a decreased shaft width results in a smaller size of the exit point for diffusing molecules from the node. This is similar to e.g dendritic spines, which compartmentalization is increased for thinner spine necks Santamaria et al. (2011); Tonnesen et al. (2014). The geometries that we have designed can thus be considered as a reasonable approximation of the ultrastructure of the gliapil observed experimentally in live tissue.

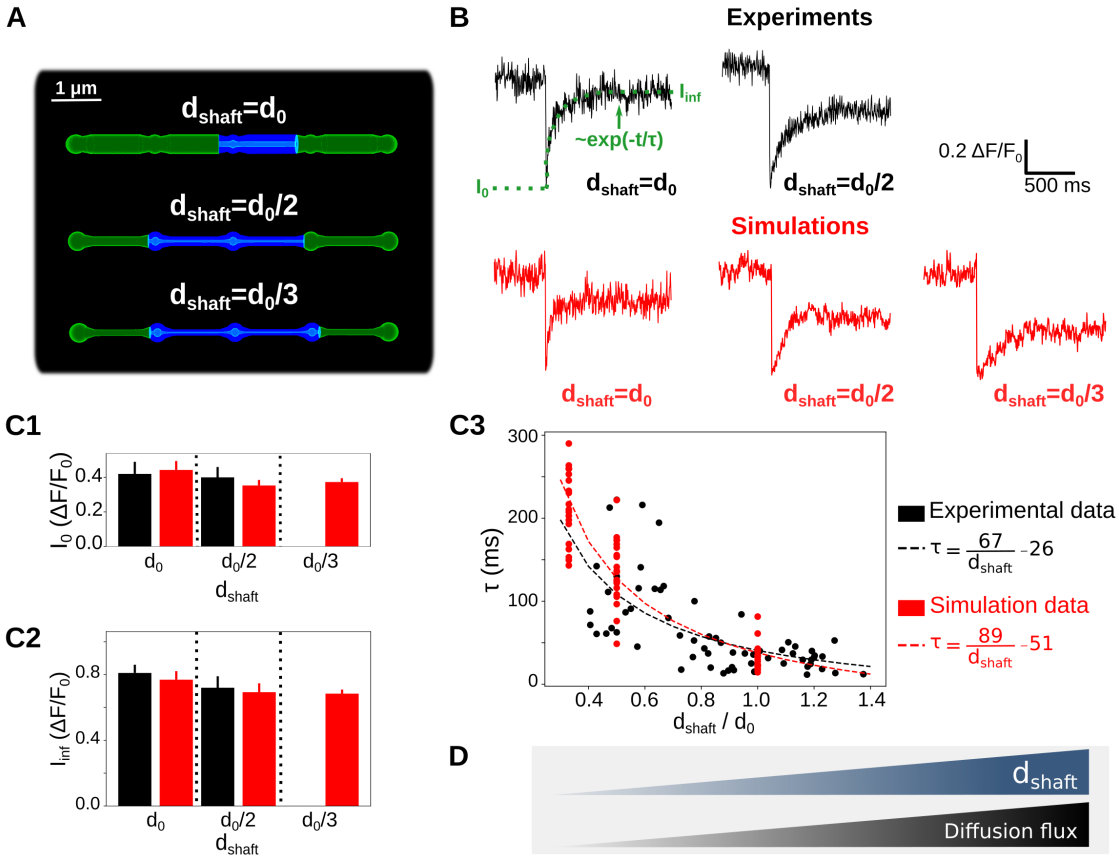

Figure 3: **Simulations confirm that thin shafts favor node compartmentalization.**

Thin shafts enhance Ca^{2+} activity in nodes

80% of astrocyte Ca^{2+} activity occurs in the gliapil Bindocci et al. (2017), which suggests that most neuron-astrocyte communication occurs at fine astrocytic processes. As we observed that a decreased shaft width is associated with a decreased diffusion flux, i.e an increased compartmentalization of nodes, we have tested whether this effect influences Ca^{2+} activity upon neuronal stimulation. To do so, we have first analyzed Ca^{2+} signals resulting from a single neuronal stimulation, which was simulated as an infusion of IP_3 and Ca^{2+} in the stimulated node, node 1 (see Methods). Those parameters encompass the IP_3 production by phospholipase C following the activation of G_q-G-protein-coupled receptors (GPCRs) resulting from the binding of neuronal glutamate, ATP and noradrenaline to G_q proteins, and Ca^{2+} entry at the plasma membrane through Ca^{2+} channels, ionotropic receptors or the sodium/calcium exchanger (NCX) functioning in reverse mode Ahmadpour et al. (2021); Semyanov et al. (2020). Signals were recorded both in the stimulated node, node 1, and in the neighboring node, node 2 (Movie S2). Representative Ca^{2+} traces in node 2 for $d_{\text{shaft}} = d_0$, $\frac{d_0}{2}$ and $\frac{d_0}{3}$ are displayed in Fig 4A. Our first result is that Ca^{2+} peak probability increases when d_{shaft} decreases (Fig 4B1). The time to 1^{st} peak increases with d_{shaft} (Fig 4B2). By contrast, peak amplitude (Fig 4B3) and duration (Fig 4B4) increase when d_{shaft} decreases. To better understand the mechanisms responsible for the increased Ca^{2+} peak probability, amplitude and duration when d_{shaft} decreases, we measured the frequency of IP_3R opening in nodes 1 and 2. The frequency of IP_3R opening increases when d_{shaft} decreases (Fig 4B5). Note that the duration of IP_3R opening and the number of IP_3Rs open per Ca^{2+} peak did not vary with d_{shaft}. The increased IP_3R opening frequency associated with small values of d_{shaft} probably results from the increased residency time of molecules in nodes connected to thin shafts (Fig 4C). Indeed, a thin shaft can "trap" Ca^{2+} and IP_3 longer in the node, thus locally increasing the probability of IP_3Rs to open, resulting in larger Ca^{2+} peaks. For more details, the reader can refer to the theoretical work investigating the narrow escape problem for diffusion in microdomains Schuss et al. (2007). Nodes connected to thinner shafts, despite being characterized by a lower diffusion flux (Fig 3), could thus consist of signal amplification units, favoring the generation of larger signals, therefore increasing Ca^{2+} peak probability, amplitude and duration both in the stimulated and in neighboring nodes.

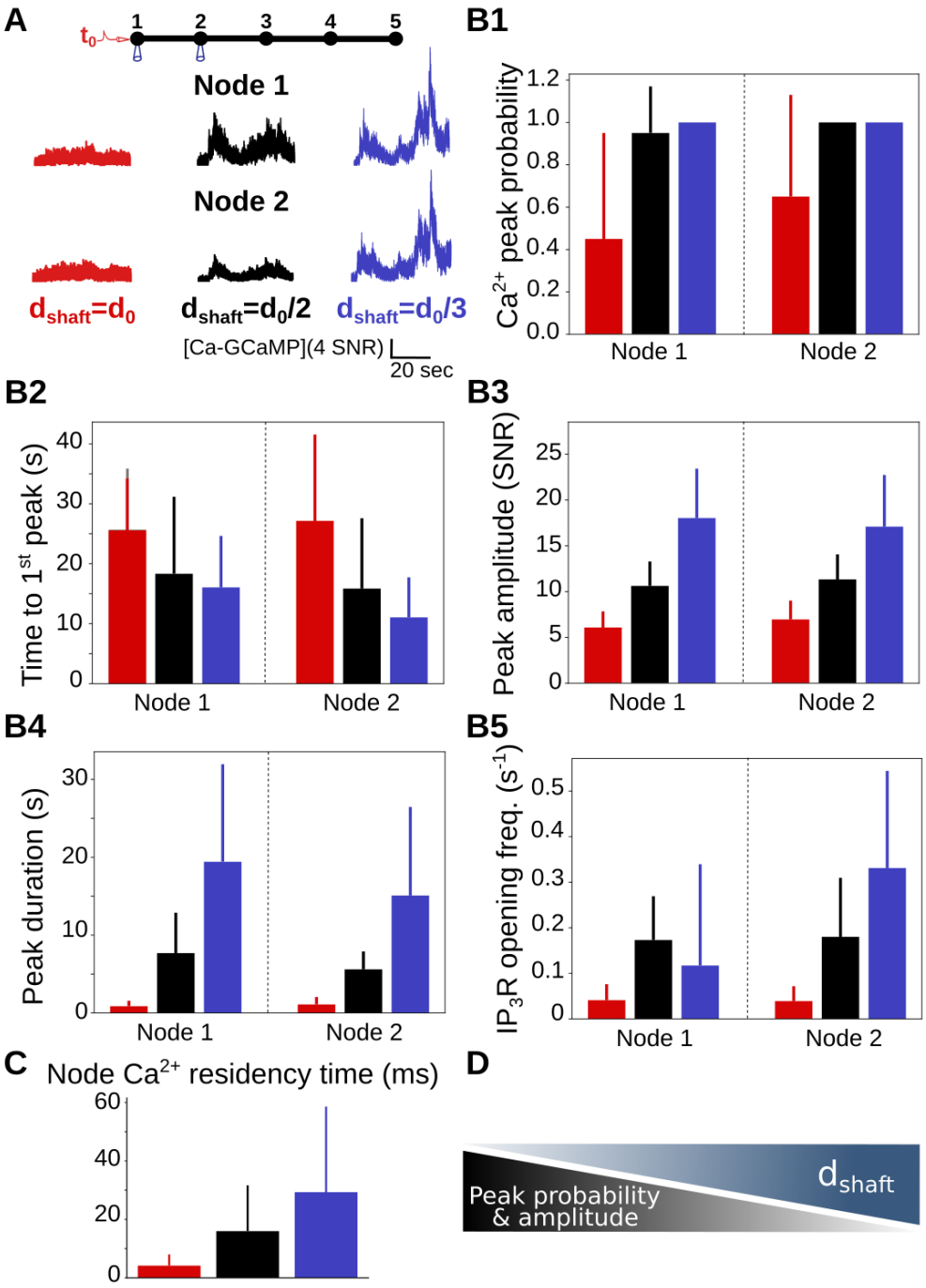

Figure 4: Ca^{2+} **peak probability, amplitude and duration increase when shaft width decreases.**

To identify the cause of the increased Ca^{2+} activity when shaft width decreases (Fig 4), we performed simulations in which we altered the stimulated node (Figure 3S2D-E), Ca^{2+} influx at the plasma membrane

(Figure S3) and boundary conditions (Figure S4). Those parameters did not affect the observed effects of d_{shaft} on Ca^{2+} dynamics. Furthermore, we repeated simulations of Fig 4 with constant cytosolic volume and constant number of IP_3Rs , irrespective of the value of d_{shaft} (Figure S5). Our results highlight that the relevant parameter responsible for the observed effects of d_{shaft} on Ca^{2+} signal characteristics is the node/shaft width ratio or the cytosolic volume rather than d_{shaft} itself. Spontaneous Ca^{2+} signals were affected by shaft width in the same way as neuronal-induced Ca^{2+} signals (Figure S6) and, in particular, reproduced the increase of the amplitude ratio of spontaneous Ca^{2+} signals between node 2 and node 1 with shaft width observed in hippocampal organotypic cultures Arizono et al. (2020). Note that ER morphology, in particular ER surface area (Figure S7, S8 and S9), and Ca^{2+} buffering by Ca^{2+} indicators (Figure S10), consistent with previous reports Denizot et al. (2019); Bartol et al. (2015); Majewska et al. (2000), also altered local Ca^{2+} activity. Overall, our results suggest that a decreased shaft width, resulting in a decreased diffusion efflux from nodes, increases Ca^{2+} peak probability, amplitude and duration. Conversely, the swelling of fine processes, resulting in an increase of shaft width, attenuates local Ca^{2+} peak probability, amplitude and duration.

Ca^{2+} imaging confirms that swelling attenuates local spontaneous Ca^{2+} activity

To validate the role of thin shafts suggested by our model's predictions, we tried to recreate the widening of shaft width in experimental conditions. Coincidentally, our recent super-resolution study revealed that the nano-architecture of fine processes is remodeled in hypo-osmotic conditions, where shaft width increased while node width remained unaltered (see Fig 3 in Arizono, Inavalli, et al. (2021)). While hypo-osmotic conditions undoubtedly cause many physiological changes to astrocytes, it is the closest experimentally available model to test our model predictions. We thus performed experimental measurements of Ca^{2+} activity in fine astrocytic processes under basal and hypo-osmotic conditions. To record Ca^{2+} signals in fine branchlets, we used confocal microscopy in organotypic cultures, which provide a high level of optical access and sample stability in live tissue (resolution $\approx$ 200 nm in x-y versus $\approx$ 500 nm for two-photon microscopy). In accordance with our model's predictions, Ca^{2+} peak amplitude and duration were lower in hypo-osmotic compared to basal conditions (Fig 5A-D). Such differences were not observed in the absence of HOC (Fig 5E-F). Overall, our experimental results confirm that the complex nano-architecture of fine astrocytic processes and its alteration, such as cell swelling, shapes local Ca^{2+} activity.

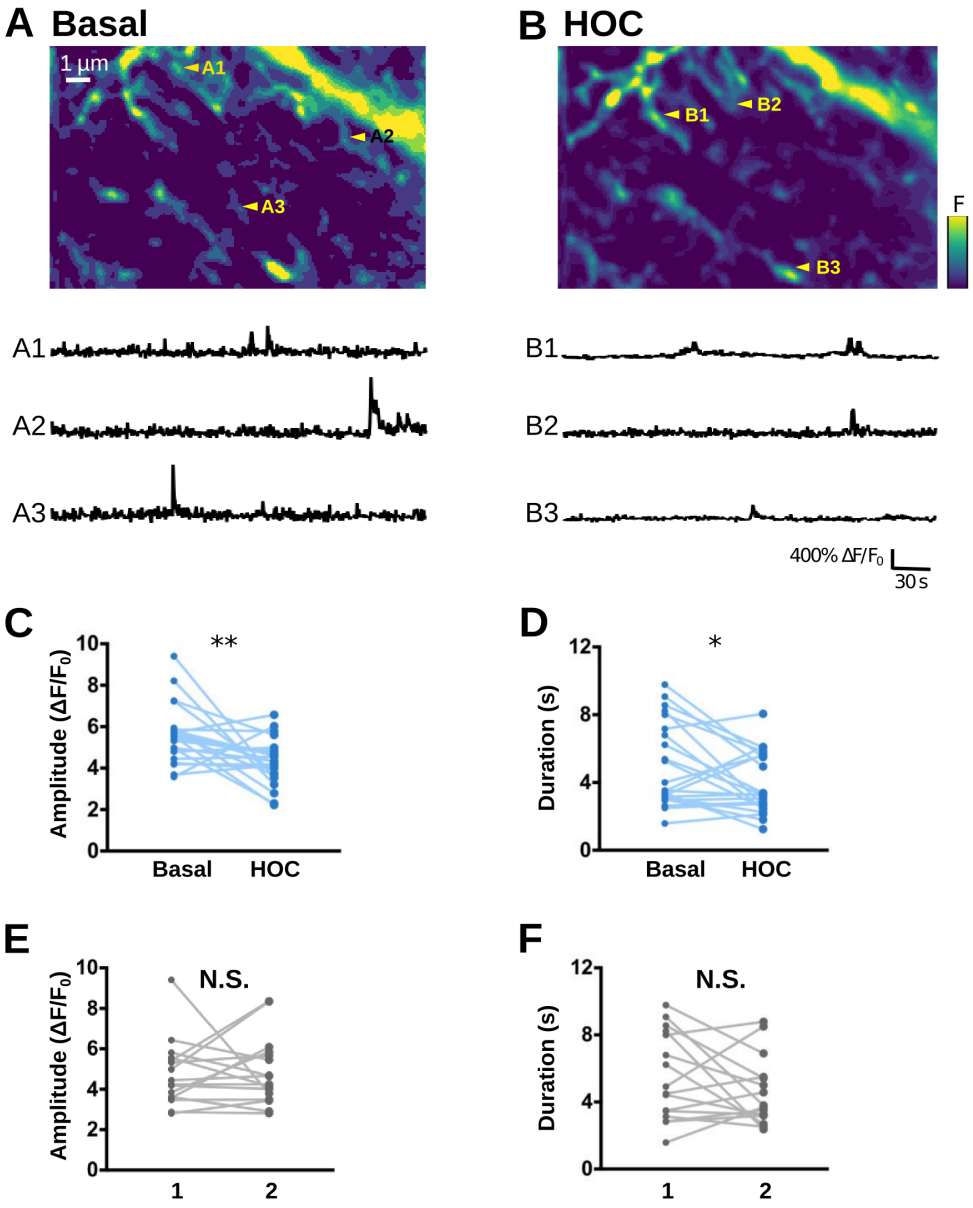

Figure 5: Ca^{2+} **imaging confirms that swelling attenuates local spontaneous** Ca^{2+} **activity.**

Thin shafts favor more robust signal propagation

As a single branchlet communicates with multiple dendritic spines, which can function independently or belong to a cluster of co-active synapses Arizono et al. (2020); Reichenbach et al. (2010); Witcher et al. (2007); Cali et al. (2019); Semyanov et al. (2020), the frequency of node stimulation within the branchlet can vary drastically. Thus, we have tested how node stimulation frequency affects Ca^{2+} activity in the

branchlet. To do so, we have performed simulations in which neighboring nodes were repeatedly stimulated after a time period τ_{IP3}, that varied from 50 ms to 5 s, while Ca^{2+} signals were recorded in a remote node, node 5 (Fig 6A). Neuronal stimulation is simulated as an infusion of 50 IP_3 molecules in the stimulated node. Representative Ca^{2+} traces in node 5 in branchlets with various shaft widths d_{shaft} are presented in Fig 6A for τ_{IP3}=250 and 3000 ms. Our first notable result is that the time to 1^{st} peak in node 5 decreases with d_{shaft} , whatever the value of τ_{IP3} (Fig 6B1). More specifically, time to 1^{st} peak is higher for $d_{shaft} = d_0$ compared to both $d_{shaft} = \frac{d_0}{2}$ and $\frac{d_0}{3}$, while differences between $d_{shaft} = \frac{d_0}{2}$ and $\frac{d_0}{3}$ are not as striking. Moreover, the difference between $d_{shaft} = d_0$, $\frac{d_0}{2}$ and $\frac{d_0}{3}$ increases with τ_{IP3}. This suggests that geometries with $d_{shaft} = d_0$ better discriminate slow from fast frequency of node stimulation compared to geometries with thinner shafts. Geometries with $d_{shaft} = d_0$ are further characterized by a lower Ca^{2+} peak probability in node 5 compared to geometries with $d_{shaft} = \frac{d_0}{2}$ and $\frac{d_0}{3}$ (Fig 6B2). More precisely, Ca^{2+} peak probability decreases as τ_{IP3} increases for $d_{shaft} = d_0$, which was observed independently of our boundary conditions (Figure S11, see Methods). This suggests that geometries with larger shafts could be associated with decreased signal propagation to remote nodes in case of repeated node stimulation at low frequency ($\tau_{IP3} > 2$ s).

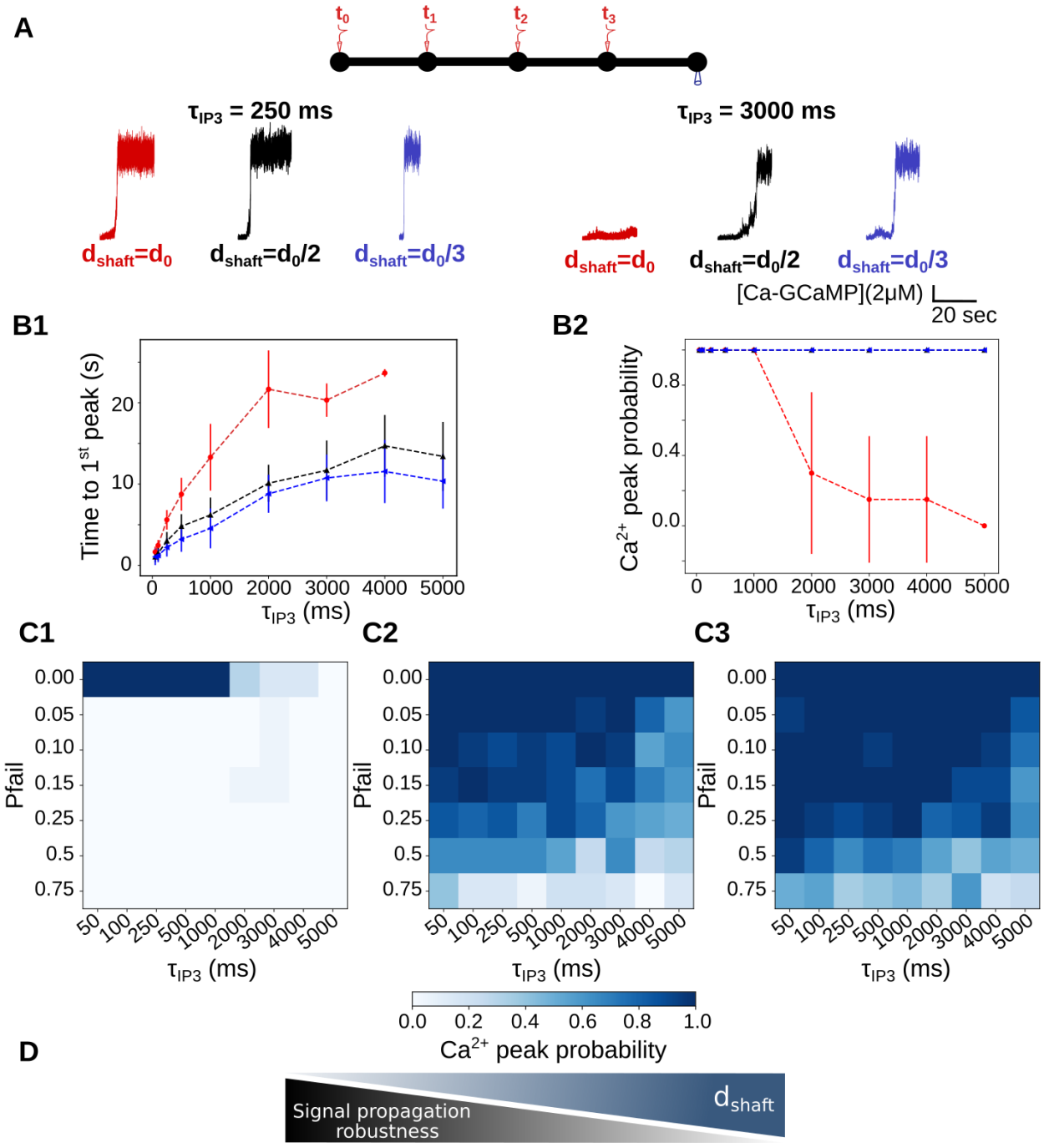

Figure 6: **Thin shafts favor a more robust signal propagation upon repeated neurotransmitter release events.**

For τ_{IP3}=4s and $d_{shaft} = \frac{d_0}{3}$, signals were detected in node 5 11.55 ± 3.89 s after the stimulation of node 1, which means that they occurred before the stimulation of node 4 (t=t_0 + 12s for τ_{IP3}=4s). This

phenomenon was not observed for $d_{shaft} = d_0$, for which time to 1st peak when τ_{IP3}=4s was 23.67 ± 0.47 s. This suggests that for $d_{shaft} = \frac{d_0}{3}$, contrary to $d_{shaft} = d_0$, one node stimulation could be omitted without having any consequence on Ca^{2+} peak probability in node 5. In order to test this hypothesis, we have performed simulations in which the stimulation of nodes 2, 3 and 4 occurred with a given probability of failure p_{fail}. Simulations were performed for p_{fail}=0, 0.05, 0.1, 0.15, 0.25 and 0.75. Ca^{2+} peak probability in node 5, depending on p_{fail} and on τ_{IP3} is presented in Fig 6C, for $d_{shaft} = d_0$ (Fig 6C1), $d_{shaft} = \frac{d_0}{2}$ (Fig 6C2) and $d_{shaft} = \frac{d_0}{3}$(Fig 6C3). As expected, Ca^{2+} peak probability, despite high values of p_{fail}, increases when d_{shaft} decreases. Thus, thin shafts can favor signal propagation by allowing the omission of a node stimulation. In that sense, geometries displaying thin shafts are characterized by a more robust signal propagation (Fig 6D).

Together, our results suggest that, in the context of repeated node stimulation, thin shafts are associated with an increase of Ca^{2+} peak probability in more remote nodes, with an earlier signal onset, suggesting increased signal propagation. Astrocytic processes with thicker shafts (here $d_{shaft} = d_0$), such as observed in hypo-osmotic conditions Arizono, Inavalli, et al. (2021), are associated with lower signal propagation in case of low stimulation frequency (time period > 2 s), potentially favoring the formation of local Ca^{2+} hotspots. Our results suggest that geometries with thick shafts could impair signal propagation when a branchlet is stimulated at a low frequency. In that sense, astrocyte branchlets with thicker shafts would be better detectors of the surrounding level of neuronal activity. By contrast, branchlets with thin shafts would be less discriminating and provide more robust signal propagation.

Discussion

Fine astrocytic processes are responsible for most astrocytic Ca^{2+} signals Bindocci et al. (2017) and are preferential sites of neuron-astrocyte communication Arizono et al. (2020). A better understanding of the mechanistic link between their morphology and the spatio-temporal properties of local Ca^{2+} signals is crucial, yet hard to test experimentally. Here, we perform reaction-diffusion simulations in idealized morphologies of astrocytic processes derived from 3D super-resolution microscopy to investigate the effect of astrocyte nanoscale morphology on Ca^{2+} activity in the gliapil. Our simulation results indicate that the nanoscale morphological features of astrocytic processes effectively increase the peak probability, duration, amplitude and propagation of Ca^{2+} signals. Conversely, the alteration of the node-shaft arrangement of the spongiform domain associated with astrocyte swelling attenuates local Ca^{2+} activity and signal propagation (Fig **??**). Our simulation results, in accordance with experimental data, suggest that thin

shafts effectively decrease diffusion flux, resulting in an increased compartmentalization of biochemical signals in nodes. Thus, nodes, similarly to dendritic spines Santamaria et al. (2011), act as diffusion traps when shaft width is low. Note that, more than the value of shaft width itself, our results emphasize the effect of the ratio between node and shaft diameter on Ca^{2+} activity. The simple geometries that we have evaluated in this study could be used to build a more comprehensive model of the spongiform structure to simulate Ca^{2+} activity in the entire astrocyte. By recording the molecular interactions resulting in Ca^{2+} signals upon neuronal stimulation in small cellular compartments of the gliapil, which cannot be performed experimentally, our simulation results shed light on the mechanisms by which the nano-architecture of astrocytic processes influences the frequency, amplitude and propagation of local Ca^{2+} signals at tripartite synapses in health and disease.

Experimental Ca^{2+} recordings of astrocyte activity have established that astrocyte processes display both highly localized microdomain signals and propagating Ca^{2+} waves Srinivasan et al. (2015); Bindocci et al. (2017). Our simulations suggest that the morphology of the cell and of its organelles can strongly influence the formation of these patterns of astrocytic Ca^{2+} signaling. Notably, thinner shafts allow less discriminating and more robust signal propagation upon repeated stimuli compared to larger shafts. On the contrary, geometries with thick shafts seem to be more discriminating, potentially favoring the propagation of signals resulting from repeated stimuli from co-active synapses. Cellular morphology thus emerges as a key parameter that regulates the active propagation of Ca^{2+} signals. The ultrastructure of the spongiform domain of astrocytes is very complex, characterized by abundant branching points, conferring a reticular morphology Arizono et al. (2020). Those branching points are reportedly sometimes arranged into ring-like structures, although their occurrence and shape are still debated and could differ depending on the brain region under study Arizono et al. (2020); Panatier et al. (2014); Kiyoshi et al. (2020); Salmon et al. (2021); Arizono & Nägerl (2021). The effect of this reticular ultrastructure on the propagation of Ca^{2+} signals remains to be uncovered. Further characterization of the shape of fine astrocytic processes of the spongiform domain, their variability as well as their connectivity to the neighboring synapses are thus required. Pairing those observations with biophysically-detailed models such as the one presented in this study stands to deepen our understanding of the roles of astrocytic and neuronal morphology at tripartite synapses on neuron-astrocyte communication.

In neurons, both experimental Yuste et al. (2000); Noguchi et al. (2005); Tonnesen et al. (2014) and

modelling Schmidt & Eilers (2009); Biess et al. (2007); Simon et al. (2014); Bell et al. (2019); Holcman & Schuss (2005, 2011); Santamaria et al. (2011); Cugno et al. (2019) studies have suggested that thin spine necks favor the compartmentalization of Ca^{2+} signals within the spine head. This compartmentalization of synapses allows neurons to discriminate various inputs and to process information locally Wybo et al. (2019); Poirazi & Papoutsi (2020), increasing the computational power of the neuronal circuits. According to our simulation results, nodes connected to thin shafts could favor the emergence of large signals at the site of neuron-astrocyte communication. Interestingly, we further propose that those amplified signals in nodes, instead of resulting in Ca^{2+} hotspots, favor active signal propagation. Fine astrocytic processes encounter morphological rearrangements that are activity-dependent, which notably influence synaptic maturation, efficacy and spine stability Theodosis et al. (2008); Zhou et al. (2019); Henneberger et al. (2020). Our study sheds light on the influence of rearrangements of the reticular morphology of fine processes on signal computation by astrocytes. Further investigation manipulating astrocyte morphology *in situ* as well as *in vivo* is required to better characterize the variability of astrocyte ultrastructure and the associated integration of Ca^{2+} signals.

The morphology of the complex spongiform domain of astrocytes is highly dynamic, subject to activity-dependent as well as pathological remodeling. Our study, providing mechanisms by which an altered astrocyte morphology influences neuron-astrocyte communication at the nanoscale, gives new insights into the involvement of astrocytes in brain function in health and disease.

References

Agarwal, A., Wu, P.-H., Hughes, E. G., Fukaya, M., Tischfield, M. A., Langseth, A. J., ... Bergles, D. E. (2017, February). Transient Opening of the Mitochondrial Permeability Transition Pore Induces Microdomain Calcium Transients in Astrocyte Processes. *Neuron*, *93*(3), 587–605.e7. Retrieved 2017-06-29, from `http://www.cell.com/neuron/abstract/S0896-6273(16)31007-8` doi: 10.1016/j.neuron.2016.12.034

Ahmadpour, N., Kantroo, M., & Stobart, J. L. (2021, October). Extracellular Calcium Influx Pathways in Astrocyte Calcium Microdomain Physiology. *Biomolecules*, *11*(10), 1467. Retrieved 2021-10-14, from `https://www.mdpi.com/2218-273X/11/10/1467` (Number: 10 Publisher: Multidisciplinary Digital Publishing Institute) doi: 10.3390/biom11101467

Arizono, M., Bancelin, S., Bethge, P., Chéreau, R., Idziak, A., Inavalli, V. V. G. K., ... Nägerl, U. V. (2021, March). Nanoscale imaging of the functional anatomy of the brain. *Neuroforum*. Retrieved 2021-04-02, from `https://www.degruyter.com/document/doi/10.1515/nf-2021-0004/html` (Publisher: De Gruyter Section: Neuroforum) doi: 10.1515/nf-2021-0004

Arizono, M., Inavalli, V. V. G. K., Bancelin, S., Fernández-Monreal, M., & Nägerl, U. V. (2021). Super-resolution shadow imaging reveals local remodeling of astrocytic microstructures and brain extracellular space after osmotic challenge. *Glia*, *69*(6), 1605–1613. Retrieved 2021-06-11, from `https://onlinelibrary.wiley.com/doi/abs/10.1002/glia.23995` (_eprint: https://onlinelibrary.wiley.com/doi/pdf/10.1002/glia.23995) doi: 10.1002/glia.23995

Arizono, M., Inavalli, V. V. G. K., Panatier, A., Pfeiffer, T., Angibaud, J., Levet, F., ... Nägerl, U. V. (2020, April). Structural basis of astrocytic Ca 2+ signals at tripartite synapses. *Nature Communications*, *11*(1), 1–15. Retrieved 2020-04-21, from `https://www.nature.com/articles/s41467-020-15648-4` (Number: 1 Publisher: Nature Publishing Group) doi: 10.1038/s41467-020-15648-4

Arizono, M., & Nägerl, U. V. (2021). Deciphering the functional nano-anatomy of the tripartite synapse using stimulated emission depletion microscopy. *Glia*, *n/a*(n/a). Retrieved

2021-10-21, from https://onlinelibrary.wiley.com/doi/abs/10.1002/glia.24103 (_eprint: https://onlinelibrary.wiley.com/doi/pdf/10.1002/glia.24103) doi: 10.1002/glia.24103

Bartol, T. M., Keller, D. X., Kinney, J. P., Bajaj, C. L., Harris, K. M., Sejnowski, T. J., & Kennedy, M. B. (2015, October). Computational reconstitution of spine calcium transients from individual proteins. *Frontiers in Synaptic Neuroscience*, *7*. Retrieved 2018-04-14, from https://www.ncbi.nlm.nih.gov/pmc/articles/PMC4595661/ doi: 10.3389/fnsyn.2015.00017

Bell, M., Bartol, T., Sejnowski, T., & Rangamani, P. (2019, August). Dendritic spine geometry and spine apparatus organization govern the spatiotemporal dynamics of calcium. *The Journal of General Physiology*, *151*(8), 1017–1034. Retrieved 2019-09-27, from http://jgp.rupress.org/content/151/8/1017 doi: 10.1085/jgp.201812261

Bezprozvanny, I., Watras, J., & Ehrlich, B. E. (1991, June). Bell-shaped calcium-response curves of Ins(1,4,5)P3- and calcium-gated channels from endoplasmic reticulum of cerebellum. *Nature*, *351*(6329), 751–754. doi: 10.1038/351751a0

Biess, A., Korkotian, E., & Holcman, D. (2007, August). Diffusion in a dendritic spine: The role of geometry. *Physical Review E*, *76*(2), 021922. Retrieved 2020-04-22, from https://link.aps.org/doi/10.1103/PhysRevE.76.021922 (Publisher: American Physical Society) doi: 10.1103/PhysRevE.76.021922

Bindocci, E., Savtchouk, I., Liaudet, N., Becker, D., Carriero, G., & Volterra, A. (2017, May). Three-dimensional Ca^{2+} imaging advances understanding of astrocyte biology. *Science*, *356*(6339), eaai8185. Retrieved 2017-06-27, from http://science.sciencemag.org/content/356/6339/eaai8185 doi: 10.1126/science.aai8185

Brazhe, A. R., Postnov, D. E., & Sosnovtseva, O. (2018, October). Astrocyte calcium signaling: Interplay between structural and dynamical patterns. *Chaos: An Interdisciplinary Journal of Nonlinear Science*, *28*(10), 106320. Retrieved 2018-10-23, from https://aip.scitation.org/doi/abs/10.1063/1.5037153 doi: 10.1063/1.5037153

509 Bushong, E. A., Martone, M. E., Jones, Y. Z., & Ellisman, M. H. (2002, January). Protoplas-
510 mic astrocytes in CA1 stratum radiatum occupy separate anatomical domains. *The Journal of*
511 *Neuroscience: The Official Journal of the Society for Neuroscience*, *22*(1), 183–192.

512 Cali, C., Agus, M., Kare, K., Boges, D. J., Lehvaslaiho, H., Hadwiger, M., & Magistretti, P. J.
513 (2019, September). 3D cellular reconstruction of cortical glia and parenchymal morphometric
514 analysis from Serial Block-Face Electron Microscopy of juvenile rat. *Progress in Neurobiology*,
515 101696. Retrieved 2019-09-24, from `http://www.sciencedirect.com/science/article/pii/`
516 `S0301008219300139` doi: 10.1016/j.pneurobio.2019.101696

517 Cugno, A., Bartol, T. M., Sejnowski, T. J., Iyengar, R., & Rangamani, P. (2019, August). Geometric
518 principles of second messenger dynamics in dendritic spines. *Scientific Reports*, *9*(1), 1–18. Re-
519 trieved 2020-04-22, from `https://www.nature.com/articles/s41598-019-48028-0` (Number:
520 1 Publisher: Nature Publishing Group) doi: 10.1038/s41598-019-48028-0

521 Denizot, A., Arizono, M., Nägerl, U. V., Soula, H., & Berry, H. (2019, August). Simulation of
522 calcium signaling in fine astrocytic processes: Effect of spatial properties on spontaneous activity.
523 *PLOS Computational Biology*, *15*(8), e1006795. Retrieved 2019-08-27, from `https://journals`
524 `.plos.org/ploscompbiol/article?id=10.1371/journal.pcbi.1006795` doi: 10.1371/journal
525 .pcbi.1006795

526 De Young, G. W., & Keizer, J. (1992, October). A single-pool inositol 1,4,5-trisphosphate-receptor-
527 based model for agonist-stimulated oscillations in Ca2+ concentration. *Proceedings of the National*
528 *Academy of Sciences*, *89*(20), 9895–9899. Retrieved 2016-12-15, from `http://www.pnas.org/`
529 `cgi/doi/10.1073/pnas.89.20.9895` doi: 10.1073/pnas.89.20.9895

530 Di Castro, M. A., Chuquet, J., Liaudet, N., Bhaukaurally, K., Santello, M., Bouvier, D., ... Volterra,
531 A. (2011, October). Local Ca2+ detection and modulation of synaptic release by astrocytes.
532 *Nature Neuroscience*, *14*(10), 1276–1284. doi: 10.1038/nn.2929

533 Giaume, C., & Venance, L. (1998, September). Intercellular calcium signaling and gap
534 junctional communication in astrocytes. *Glia*, *24*(1), 50–64. Retrieved from `http://`

onlinelibrary.wiley.com.insb.bib.cnrs.fr/doi/10.1002/(SICI)1098-1136(199809)24:1<50::AID-GLIA6>3.0.CO;2-4/abstract doi: 10.1002/(SICI)1098-1136(199809)24:1<50::AID-GLIA6>3.0.CO;2-4

Gillespie, D. T. (1977, December). Exact stochastic simulation of coupled chemical reactions. *The Journal of Physical Chemistry*, *81*(25), 2340–2361. Retrieved 2018-04-20, from https://doi.org/10.1021/j100540a008 doi: 10.1021/j100540a008

Grosche, J., Matyash, V., Möller, T., Verkhratsky, A., Reichenbach, A., & Kettenmann, H. (1999, February). Microdomains for neuron–glia interaction: parallel fiber signaling to Bergmann glial cells. *Nature Neuroscience*, *2*(2), 139–143. Retrieved 2019-02-13, from https://www.nature.com/articles/nn0299_139 doi: 10.1038/5692

Gähwiler, B. H. (1981, December). Organotypic monolayer cultures of nervous tissue. *Journal of Neuroscience Methods*, *4*(4), 329–342. Retrieved 2018-05-04, from http://www.sciencedirect.com/science/article/pii/0165027081900030 doi: 10.1016/0165-0270(81)90003-0

Haustein, M. D., Kracun, S., Lu, X.-H., Shih, T., Jackson-Weaver, O., Tong, X., ... Khakh, B. S. (2014, April). Conditions and constraints for astrocyte calcium signaling in the hippocampal mossy fiber pathway. *Neuron*, *82*(2), 413–429. doi: 10.1016/j.neuron.2014.02.041

Henneberger, C., Bard, L., Panatier, A., Reynolds, J. P., Kopach, O., Medvedev, N. I., ... Rusakov, D. A. (2020, September). LTP Induction Boosts Glutamate Spillover by Driving Withdrawal of Perisynaptic Astroglia. *Neuron*. Retrieved 2020-10-15, from http://www.sciencedirect.com/science/article/pii/S0896627320306619 doi: 10.1016/j.neuron.2020.08.030

Hepburn, I., Chen, W., Wils, S., & De Schutter, E. (2012). STEPS: efficient simulation of stochastic reaction–diffusion models in realistic morphologies. *BMC Systems Biology*, *6*(1), 36. Retrieved 2017-02-03, from http://bmcsystbiol.biomedcentral.com/articles/10.1186/1752-0509-6-36 doi: 10.1186/1752-0509-6-36

Holcman, D., & Schuss, Z. (2005, January). Modeling Calcium Dynamics in Dendritic Spines. *SIAM Journal on Applied Mathematics*, *65*(3), 1006–1026. Retrieved 2019-03-26, from https://

epubs.siam.org/doi/abs/10.1137/S003613990342894X doi: 10.1137/S003613990342894X

Holcman, D., & Schuss, Z. (2011, October). Diffusion laws in dendritic spines. *The Journal of Mathematical Neuroscience*, *1*(1), 10. Retrieved 2019-04-09, from https://doi.org/10.1186/2190-8567-1-10 doi: 10.1186/2190-8567-1-10

Isaacson, S. A., & Isaacson, D. (2009, December). The Reaction-Diffusion Master Equation, Diffusion Limited Reactions, and Singular Potentials. *Physical Review. E, Statistical, Nonlinear, and Soft Matter Physics*, *80*(6 Pt 2), 066106. Retrieved from http://www.ncbi.nlm.nih.gov/pmc/articles/PMC3405976/

Kiyoshi, C. M., Aten, S., Arzola, E. P., Patterson, J. A., Taylor, A. T., Du, Y., ... Zhou, M. (2020, October). Ultrastructural view of astrocyte-astrocyte and astrocyte-synapse contacts within the hippocampus. *bioRxiv*, 2020.10.28.358200. Retrieved 2021-02-05, from https://www.biorxiv.org/content/10.1101/2020.10.28.358200v1 (Publisher: Cold Spring Harbor Laboratory Section: New Results) doi: 10.1101/2020.10.28.358200

Lafrenaye, A. D., & Simard, J. M. (2019, January). Bursting at the Seams: Molecular Mechanisms Mediating Astrocyte Swelling. *International Journal of Molecular Sciences*, *20*(2), 330. Retrieved 2021-06-09, from https://www.mdpi.com/1422-0067/20/2/330 (Number: 2 Publisher: Multidisciplinary Digital Publishing Institute) doi: 10.3390/ijms20020330

Lee, H.-G., Wheeler, M. A., & Quintana, F. J. (2022, February). Function and therapeutic value of astrocytes in neurological diseases. *Nature Reviews Drug Discovery*, 1–20. Retrieved 2022-02-20, from https://www.nature.com/articles/s41573-022-00390-x (Publisher: Nature Publishing Group) doi: 10.1038/s41573-022-00390-x

Lind, B. L., Brazhe, A. R., Jessen, S. B., Tan, F. C. C., & Lauritzen, M. J. (2013, November). Rapid stimulus-evoked astrocyte Ca2+ elevations and hemodynamic responses in mouse somatosensory cortex in vivo. *Proceedings of the National Academy of Sciences*, 201310065. Retrieved 2018-02-26, from http://www.pnas.org/content/early/2013/11/08/1310065110 doi: 10.1073/pnas.1310065110

587 Majewska, A., Brown, E., Ross, J., & Yuste, R. (2000, March). Mechanisms of Calcium Decay
588 Kinetics in Hippocampal Spines: Role of Spine Calcium Pumps and Calcium Diffusion through
589 the Spine Neck in Biochemical Compartmentalization. *Journal of Neuroscience*, *20*(5), 1722–
590 1734. Retrieved 2018-11-23, from `http://www.jneurosci.org/content/20/5/1722` doi: 10
591 .1523/JNEUROSCI.20-05-01722.2000

592 McDougal, R. A., Morse, T. M., Carnevale, T., Marenco, L., Wang, R., Migliore, M., ... Hines,
593 M. L. (2017, February). Twenty years of ModelDB and beyond: building essential modeling
594 tools for the future of neuroscience. *Journal of Computational Neuroscience*, *42*(1), 1–10. doi:
595 10.1007/s10827-016-0623-7

596 Nedergaard, M., Rodríguez, J. J., & Verkhratsky, A. (2010, February). Glial calcium and diseases
597 of the nervous system. *Cell Calcium*, *47*(2), 140–149. doi: 10.1016/j.ceca.2009.11.010

598 Noguchi, J., Matsuzaki, M., Ellis-Davies, G. C. R., & Kasai, H. (2005, May). Spine-Neck Ge-
599 ometry Determines NMDA Receptor-Dependent Ca2+ Signaling in Dendrites. *Neuron*, *46*(4),
600 609–622. Retrieved 2020-04-22, from `http://www.sciencedirect.com/science/article/pii/`
601 `S0896627305002382` doi: 10.1016/j.neuron.2005.03.015

602 Otsu, Y., Couchman, K., Lyons, D. G., Collot, M., Agarwal, A., Mallet, J.-M., ... Charpak, S.
603 (2015, February). Calcium dynamics in astrocyte processes during neurovascular coupling. *Na-*
604 *ture Neuroscience*, *18*(2), 210–218. Retrieved 2017-03-17, from `http://www.nature.com/neuro/`
605 `journal/v18/n2/full/nn.3906.html` doi: 10.1038/nn.3906

606 Panatier, A., Arizono, M., & Nägerl, U. V. (2014, October). Dissecting tripartite synapses with
607 STED microscopy. *Phil. Trans. R. Soc. B*, *369*(1654), 20130597. Retrieved 2017-04-04, from
608 `http://rstb.royalsocietypublishing.org/content/369/1654/20130597` doi: 10.1098/rstb
609 .2013.0597

610 Panatier, A., Vallée, J., Haber, M., Murai, K. K., Lacaille, J.-C., & Robitaille, R. (2011, September).
611 Astrocytes are endogenous regulators of basal transmission at central synapses. *Cell*, *146*(5), 785–
612 798. doi: 10.1016/j.cell.2011.07.022

Poirazi, P., & Papoutsi, A. (2020, June). Illuminating dendritic function with computational models. *Nature Reviews Neuroscience*, *21*(6), 303–321. Retrieved 2021-06-09, from https://www.nature.com/articles/s41583-020-0301-7 (Number: 6 Publisher: Nature Publishing Group) doi: 10.1038/s41583-020-0301-7

Reichenbach, A., Derouiche, A., & Kirchhoff, F. (2010, May). Morphology and dynamics of perisynaptic glia. *Brain Research Reviews*, *63*(1-2), 11–25. doi: 10.1016/j.brainresrev.2010.02.003

Rusakov, D. A. (2015, April). Disentangling calcium-driven astrocyte physiology. *Nature Reviews Neuroscience*, *16*(4), 226–233. Retrieved 2017-03-11, from http://www.nature.com/nrn/journal/v16/n4/full/nrn3878.html doi: 10.1038/nrn3878

Salmon, C. K., Syed, T. A., Kacerovsky, J. B., Alivodej, N., Schober, A. L., Pratte, M. T., ... Murai, K. K. (2021, November). *Organizing Principles of Astrocytic Nanoarchitecture in the Mouse Cerebral Cortex* (Tech. Rep.). Retrieved 2021-11-08, from https://www.biorxiv.org/content/10.1101/2021.11.05.467391v1 (Company: Cold Spring Harbor Laboratory Distributor: Cold Spring Harbor Laboratory Label: Cold Spring Harbor Laboratory Section: New Results Type: article) doi: 10.1101/2021.11.05.467391

Santamaria, F., Wils, S., De Schutter, E., & Augustine, G. J. (2011, August). The diffusional properties of dendrites depend on the density of dendritic spines. *The European Journal of Neuroscience*, *34*(4), 561–568. doi: 10.1111/j.1460-9568.2011.07785.x

Schmidt, H., & Eilers, J. (2009, October). Spine neck geometry determines spino-dendritic cross-talk in the presence of mobile endogenous calcium binding proteins. *Journal of Computational Neuroscience*, *27*(2), 229–243. Retrieved 2020-04-21, from https://doi.org/10.1007/s10827-009-0139-5 doi: 10.1007/s10827-009-0139-5

Schuss, Z., Singer, A., & Holcman, D. (2007, October). The narrow escape problem for diffusion in cellular microdomains. *Proceedings of the National Academy of Sciences*, *104*(41), 16098–16103. Retrieved 2021-01-25, from https://www.pnas.org/content/104/41/16098 (Publisher: National Academy of Sciences Section: Physical Sciences) doi: 10.1073/pnas.0706599104

639 Semyanov, A., Henneberger, C., & Agarwal, A. (2020, September). Making sense of astrocytic cal-
640 cium signals — from acquisition to interpretation. *Nature Reviews Neuroscience*, 1–14. Retrieved
641 2020-09-04, from `https://www.nature.com/articles/s41583-020-0361-8` (Publisher: Nature
642 Publishing Group) doi: 10.1038/s41583-020-0361-8

643 Sherwood, M. W., Arizono, M., Hisatsune, C., Bannai, H., Ebisui, E., Sherwood, J. L., ...
644 Mikoshiba, K. (2017, March). Astrocytic IP3Rs: Contribution to Ca2+ signalling and hippocam-
645 pal LTP. *Glia*, *65*(3), 502–513. Retrieved 2017-03-27, from `http://onlinelibrary.wiley.com/`
646 `doi/10.1002/glia.23107/abstract` doi: 10.1002/glia.23107

647 Shigetomi, E., Bushong, E. A., Haustein, M. D., Tong, X., Jackson-Weaver, O., Kracun, S., ...
648 Khakh, B. S. (2013, May). Imaging calcium microdomains within entire astrocyte territories
649 and endfeet with GCaMPs expressed using adeno-associated viruses. *The Journal of General*
650 *Physiology*, *141*(5), 633–647. doi: 10.1085/jgp.201210949

651 Shigetomi, E., Patel, S., & Khakh, B. S. (2016, April). Probing the Complexities of Astrocyte
652 Calcium Signaling. *Trends in Cell Biology*, *26*(4), 300–312. doi: 10.1016/j.tcb.2016.01.003

653 Shigetomi, E., Saito, K., Sano, F., & Koizumi, S. (2019, January). Aberrant Calcium Signals in
654 Reactive Astrocytes: A Key Process in Neurological Disorders. *International Journal of Molecular*
655 *Sciences*, *20*(4), 996. Retrieved 2019-02-28, from `https://www.mdpi.com/1422-0067/20/4/996`
656 doi: 10.3390/ijms20040996

657 Simon, C. M., Hepburn, I., Chen, W., & Schutter, E. D. (2014, June). The role of dendritic spine
658 morphology in the compartmentalization and delivery of surface receptors. *Journal of Computa-*
659 *tional Neuroscience*, *36*(3), 483–497. Retrieved 2018-01-18, from `https://link.springer.com/`
660 `article/10.1007/s10827-013-0482-4` doi: 10.1007/s10827-013-0482-4

661 Smith, S., & Grima, R. (2018, May). Spatial Stochastic Intracellular Kinetics: A Review of
662 Modelling Approaches. *Bulletin of Mathematical Biology*. Retrieved 2019-02-13, from `https://`
663 `doi.org/10.1007/s11538-018-0443-1` doi: 10.1007/s11538-018-0443-1

664 Spacek, J., & Harris, K. M. (1997, January). Three-Dimensional Organization of Smooth
665 Endoplasmic Reticulum in Hippocampal CA1 Dendrites and Dendritic Spines of the Imma-
666 ture and Mature Rat. *Journal of Neuroscience*, *17*(1), 190–203. Retrieved 2018-11-23, from
667 http://www.jneurosci.org/content/17/1/190 doi: 10.1523/JNEUROSCI.17-01-00190.1997

668 Srinivasan, R., Huang, B. S., Venugopal, S., Johnston, A. D., Chai, H., Zeng, H., ... Khakh, B. S.
669 (2015, May). Ca(2+) signaling in astrocytes from Ip3r2(-/-) mice in brain slices and during startle
670 responses in vivo. *Nature Neuroscience*, *18*(5), 708–717. doi: 10.1038/nn.4001

671 Stobart, J. L., Ferrari, K. D., Barrett, M. J. P., Glück, C., Stobart, M. J., Zuend, M., & Weber,
672 B. (2018, May). Cortical Circuit Activity Evokes Rapid Astrocyte Calcium Signals on a Similar
673 Timescale to Neurons. *Neuron*, *98*(4), 726–735.e4. Retrieved 2018-06-15, from http://www
674 .sciencedirect.com/science/article/pii/S0896627318302848 doi: 10.1016/j.neuron.2018
675 .03.050

676 Stobart, J. L., Ferrari, K. D., Barrett, M. J. P., Stobart, M. J., Looser, Z. J., Saab, A. S., &
677 Weber, B. (2018, January). Long-term In Vivo Calcium Imaging of Astrocytes Reveals Distinct
678 Cellular Compartment Responses to Sensory Stimulation. *Cerebral Cortex (New York, N.Y.:*
679 *1991)*, *28*(1), 184–198. doi: 10.1093/cercor/bhw366

680 Theodosis, D. T., Poulain, D. A., & Oliet, S. H. R. (2008, July). Activity-dependent structural and
681 functional plasticity of astrocyte-neuron interactions. *Physiological Reviews*, *88*(3), 983–1008.
682 doi: 10.1152/physrev.00036.2007

683 Tonnesen, J., Katona, G., Rózsa, B., & Nägerl, U. V. (2014, May). Spine neck plasticity regulates
684 compartmentalization of synapses. *Nature Neuroscience*, *17*(5), 678–685. Retrieved 2020-04-22,
685 from https://www.nature.com/articles/nn.3682 (Number: 5 Publisher: Nature Publishing
686 Group) doi: 10.1038/nn.3682

687 Tonnesen, J., Nadrigny, F., Willig, K., Wedlich-Söldner, R., & Nägerl, U. V. (2011, November).
688 Two-Color STED Microscopy of Living Synapses Using A Single Laser-Beam Pair. *Biophysi-*

cal Journal, *101*(10), 2545–2552. Retrieved 2018-12-14, from http://www.sciencedirect.com/science/article/pii/S0006349511012008 doi: 10.1016/j.bpj.2011.10.011

Urban, N., Willig, K., Hell, S., & Nägerl, U. V. (2011, September). STED Nanoscopy of Actin Dynamics in Synapses Deep Inside Living Brain Slices. *Biophysical Journal*, *101*(5), 1277–1284. Retrieved 2018-12-14, from http://www.sciencedirect.com/science/article/pii/S000634951100885X doi: 10.1016/j.bpj.2011.07.027

Verkhratsky, A., & Nedergaard, M. (2018, January). Physiology of Astroglia. *Physiological Reviews*, *98*(1), 239–389. doi: 10.1152/physrev.00042.2016

Witcher, M. R., Kirov, S. A., & Harris, K. M. (2007, January). Plasticity of perisynaptic astroglia during synaptogenesis in the mature rat hippocampus. *Glia*, *55*(1), 13–23. doi: 10.1002/glia.20415

Wu, Y.-W., Gordleeva, S., Tang, X., Shih, P.-Y., Dembitskaya, Y., & Semyanov, A. (2018, September). Morphological profile determines the frequency of spontaneous calcium events in astrocytic processes. *bioRxiv*, 410076. Retrieved 2018-09-13, from https://www.biorxiv.org/content/early/2018/09/06/410076 doi: 10.1101/410076

Wybo, W. A. M., Torben-Nielsen, B., Nevian, T., & Gewaltig, M.-O. (2019, February). Electrical Compartmentalization in Neurons. *Cell Reports*, *26*(7), 1759–1773.e7. Retrieved 2021-06-09, from https://www.sciencedirect.com/science/article/pii/S2211124719301032 doi: 10.1016/j.celrep.2019.01.074

Yasuda, R. (2017, November). Biophysics of Biochemical Signaling in Dendritic Spines: Implications in Synaptic Plasticity. *Biophysical Journal*, *113*(10), 2152–2159. Retrieved 2020-04-22, from http://www.sciencedirect.com/science/article/pii/S000634951730855X doi: 10.1016/j.bpj.2017.07.029

Yuste, R., Majewska, A., & Holthoff, K. (2000, July). From form to function: calcium compartmentalization in dendritic spines. *Nature Neuroscience*, *3*(7), 653–659. doi: 10.1038/76609

714 Zhou, B., Zuo, Y.-X., & Jiang, R.-T. (2019, March). Astrocyte morphology: Diversity, plasticity,
715 and role in neurological diseases. *CNS neuroscience & therapeutics*. doi: 10.1111/cns.13123

Tables

Table 1: Characteristics of the geometries of astrocyte branchlets used in this study. V_{cyt} is the cytosolic volume, S_{PM} is the area of the plasma membrane and S_{ER} is the area of the ER membrane. Volumes are expressed in nm^3 and areas in nm^2. Meshes are available at `http://modeldb.yale.edu/266928`, access code: lto42@tpk3D?

Geom	V_{cyt} (nm^3)	S_{PM} (nm^2)	S_{ER} (nm^2)
"5nodes" $d_{\text{shaft}} = d_0$	6.20×10^8	7.73×10^6	2.19×10^6
"5nodes" $d_{\text{shaft}} = d_0/2$	2.63×10^8	4.95×10^6	1.28×10^6
"5nodes" $d_{\text{shaft}} = d_0/3$	1.95×10^8	4.10×10^6	9.99×10^5
"No ER" $d_{\text{shaft}} = d_0$	6.73×10^8	7.73×10^6	0.00
"No ER" $d_{\text{shaft}} = d_0/2$	2.83×10^8	4.95×10^6	0.00
"No ER" $d_{\text{shaft}} = d_0/3$	2.10×10^8	4.09×10^6	0.00
"Node ER" $d_{\text{shaft}} = d_0$	6.67×10^8	7.75×10^6	4.17×10^5
"Node ER" $d_{\text{shaft}} = d_0/2$	2.74×10^8	4.96×10^6	4.37×10^5
"Node ER" $d_{\text{shaft}} = d_0/3$	2.00×10^8	4.11×10^6	4.41×10^5
"Cyl ER" $d_{\text{shaft}} = d_0$	6.27×10^8	7.74×10^6	2.03×10^6
"Cyl ER" $d_{\text{shaft}} = d_0/2$	2.77×10^8	4.95×10^6	8.78×10^5
"Cyl ER" $d_{\text{shaft}} = d_0/3$	2.07×10^8	4.09×10^6	5.86×10^5

Figure legends

Figure 1. Geometries and kinetic scheme used for simulating Ca^{2+} dynamics in node/shaft structures of the gliapil. (A) Representative STED image showing the astrocytic spongiform domain. Zoom-in images show its anatomical units: nodes and shafts. (B) Geometries reproducing node/shaft geometries of the gliapil Arizono et al. (2020); Panatier et al. (2014) were designed. Nodes are approximated as spheres of diameter 380 nm and shafts as 1 μm-long cylinders. The geometries designed in this study, referred to as "5 nodes", contain 5 identical nodes and 4 identical shafts. Unless specified otherwise, ER geometry (black) also consists in node/shaft successions (see Methods). Geometries were characterized by different shaft widths: $d_{\text{shaft}} = d_0 = 380$ nm, $d_{\text{shaft}} = \frac{d_0}{2}$ and $d_{\text{shaft}} = \frac{d_0}{3}$. The associated cytosolic volume, plasma and ER membrane areas are presented in Table 1. (C) Biochemical processes included in the model. Ca^{2+} can enter/exit the cytosol from/to the extracellular space or the endoplasmic reticulum (ER), resulting from the activity of Ca^{2+} channels/pumps. Ca^{2+} and IP_3 diffuse in the cytosol following Brownian motion. The kinetics of IP_3R channels corresponds to the 8-state Markov model from Denizot et al. (2019), adapted from De Young & Keizer (1992); Bezprozvanny et al. (1991). When both IP_3 and Ca^{2+} are bound to IP_3R activating binding sites, the IP_3R is in open state and Ca^{2+} enters the cytosol. Ca^{2+} can activate Phospholipase C δ (PLCδ), which results in the production of IP_3. For more details, please refer to Denizot et al. (2019). Neuronal stimulation is simulated as an infusion of IP_3 in the cytosol and the opening of Ca^{2+} channels at the plasma membrane with an influx rate k_{Ca} (see Methods).

Figure 2. Simulations confirm that thin shafts favor node compartmentalization. (A) Geometries of different shaft widths d_{shaft}, $d_{\text{shaft}} = d_0$, $\frac{d_0}{2}$ and $\frac{d_0}{3}$, used in the bleaching simulations. Blue color represents the bleached volume, which varied depending on the value of d_{shaft} in order to fit experimental values of I_0 and I_{inf}. (B) Representative experimental (top) and simulation (bottom) traces for different shaft width values. I_0, I_{inf} and τ were calculated using Eq 1. Note that simulations were also performed for $d_{\text{shaft}} = \frac{d_0}{3}$. ($C$) Quantification of I_0 (C1), I_{inf} (C2) and τ (C3) values in simulations (red) compared to experiments (black). Note that no experimental data was available for $d_{\text{shaft}} = \frac{d_0}{3}$. In C1 and C2, n=5×2 and 20×3 for experiments and simulations, respectively. Data are presented as mean ± STD. In C3, n=66 and n=20×3 for experiments and simulations, respectively. τ is negatively correlated to d_{shaft} in experiments (n=66 from 7 slices; Spearman r=-0.72, p<0.001 ***) and simulations (n=60; Spearman r=-0.89, p<0.001 ***). Black and red lines represent curve fit of τ as a function of d_{shaft} of the form $\tau = a * \frac{1}{d_{\text{shaft}}} + b$ for experiments and simulations, respectively. (D) Schematic summarizing the conclusion of this figure:

diffusion flux increases with d_{shaft}. In that sense, thin shafts favor node compartmentalization. Data in panels C1 and C2 are represented as mean ± STD, n=20 for each geometry.

Figure 3. Ca^{2+} **peak probability, amplitude and duration increase when shaft width decreases.** (*A*) (*Top*) Neuronal stimulation protocol simulated for each geometry: node 1 was stimulated at t=t_0=1s, while Ca^{2+} activity was monitored in node 2. Representative Ca^{2+} traces for shaft width $d_{shaft} = d_0$ (red), $\frac{d_0}{2}$ (black) and $\frac{d_0}{3}$ (blue), expressed as SNR (see Methods). (*B*) Quantification of the effect of d_{shaft} on Ca^{2+} signal characteristics Data are represented as mean ± STD, n=20. Ca^{2+} peak probability increases (***, *B1*), Time to 1^{st} peak decreases (***, *B2*), peak amplitude (***, *B3*) and duration (***, *B4*) increase when d_{shaft} decreases. (*C*) Ca^{2+} residency time in node 1 increases when d_{shaft} decreases (***, n=300). (*D*) Schematic summarizing the main result from this figure: Ca^{2+} peak probability and amplitude increase when shaft width decreases. The effect of d_{shaft} on each Ca^{2+} signal characteristic was tested using one-way ANOVA. Significance is assigned by * for $p \leq 0.05$, ** for $p \leq 0.01$, *** for $p \leq 0.001$.

Figure 4. Ca^{2+} **imaging confirms that swelling attenuates local spontaneous** Ca^{2+} **activity.** (*A, B*) (Top) Confocal images of the astrocytic spongiform domain expressing GCaMP6s at baseline (basal, A) and in hypo-osmotic condition (HOC, B), measured in organotypic hippocampal cultures (resolution: 200 nm in x-y, 600 nm in z). (Bottom) Representative traces of spontaneous Ca^{2+} events from ROIs indicated in A (A1-A3) and B (B1-B3). (*C, D*) Ca^{2+} peak amplitude (C) and duration (D) of spontaneous Ca^{2+} events are significantly smaller in hypo-osmotic conditions (HOC) compared to basal conditions (Basal). (*E, F*) Amplitude (E) and duration (F) of spontaneous Ca^{2+} events do not significantly vary when measured twice in a row (1, 2) in the absence of HOC. Lines represent measurements in the same cell, before and after applying hypo-osmotic stress. Significance is assigned by * for $p \leq 0.05$, ** for $p \leq 0.01$, *** for $p \leq 0.001$.

Figure 5. Thin shafts favor a more robust signal propagation upon repeated neurotransmitter release events. (*A*) (*Top*) Neuronal stimulation protocol: node 1 is stimulated at t=t_0=5s, node 2 at $t_0 + \tau_{IP3}$, node 3 at $t_0 + 2\tau_{IP3}$ and node 4 at $t_0 + 3\tau_{IP3}$, k_{Ca}=0 s^{-1}. Ca^{2+} activity is recorded in node 5. (*Bottom*) Representative Ca^{2+} traces in node 5 for shaft width $d_{shaft} = d_0$ (red), $\frac{d_0}{2}$ (black) and $\frac{d_0}{3}$ (blue), with τ_{IP3}=250 ms (left) and 3000 ms (right), expressed as SNR (see Methods). (*B1*) Time to 1^{st} peak increases with τ_{IP3} for d_{shaft} =d_0 (***), $\frac{d_0}{2}$ (***) and $\frac{d_0}{3}$ (***). T-tests revealed that for any value of τ_{IP3}, time to 1^{st} peak is higher for d_{shaft} =d_0 compared to d_{shaft} =$\frac{d_0}{2}$ and $\frac{d_0}{3}$. Time to 1^{st} peak is significantly

779 higher when $d_{shaft} = \frac{d_0}{2}$ compared to $d_{shaft} = \frac{d_0}{3}$, for most values of τ_{IP3} (p=0.032 *, 0.0025 **, 0.034 *,
780 0.016 * and 0.019 * for τ_{IP3}=250, 500, 1000, 4000 and 5000 ms, respectively). (*B2*) Ca^{2+} peak probability
781 in node 5 is lower for $d_{shaft} = d_0$ compared to $d_{shaft} = \frac{d_0}{2}$ and $\frac{d_0}{3}$. Ca^{2+} peak probability decreases as τ_{IP3}
782 increases for $d_{shaft} = d_0$ (***). (*C*) Ca^{2+} peak probability in node 5 (colorbar) as a function of τ_{IP3} and of
783 the probability of failure of node stimulation p_{fail}, for $d_{shaft} = d_0$ (C1), $d_{shaft} = \frac{d_0}{2}$ (C2) and $d_{shaft} = \frac{d_0}{3}$ (C3),
784 with $p_{fail} \in [0, 1]$. (*D*) Schematic summarizing the main conclusion of this figure: decreased shaft width
785 allows signal propagation despite omitted node stimulation, thus favoring more robust signal propagation.
786 Data are represented as mean ± STD, n=20 for each value of d_{shaft} and of τ_{IP3}. Lines in panel B are guides
787 for the eyes. The effect of d_{shaft} on each Ca^{2+} signal characteristic was tested using one-way ANOVA.
788 Significance is assigned by * for $p \leq 0.05$, ** for $p \leq 0.01$, *** for $p \leq 0.001$.
789